Microelectronics Reliability 122 (2021) 114134

Contents lists available at ScienceDirect

Microelectronics Reliability

journal homepage: www.elsevier.com/locate/microrel

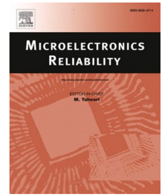

Towards virtual twin for electronic packages in automotive applications

Alexandru Prisacaru [a,c,*], Ernesto Oquelis Guerrero [a], Balakrishna Chimmineni [a], Przemyslaw Jakub Gromala [a], Yu-Hsiang Yang [b], Bongtae Han [b], Guo Qi Zhang [c]

[a] Robert Bosch GmbH, Automotive Electronics, Reutlingen 72703, Germany
[b] Mechanical Engineering Department, University of Maryland, College Park, MD 20742, USA
[c] Microelectronics Department, Delft University of Technology, Delft 2600, Netherlands

ARTICLE INFO

Keywords:
Digital twin
Machine learning
Finite element method
Surrogate modelling
Electronic package
Mechanical stress sensor

ABSTRACT

The piezoresistive silicon based stress sensor has the potential to be part of the Digital Twin implementation in automotive electronics. One solution to enforce reliability in digital twins is the use of Machine Learning (ML). One or more physical parameters are being monitored, while other parameters are projected with surrogate models, just like virtual sensors. Piezo-resistive stress sensors are employed to measure the internal stresses of electronic packages, an Acquisition Unit (AU) to read out sensor data and a Raspberry Pi to perform evaluation. Accelerated tests in air thermal chamber are performed to get time series data of the stress sensor signals, with which we can know better about how delamination develops inside the package. In this study stress measurements are performed in several electronic packages during the delamination. The delamination is detected by the stress sensor due to the continuous change of the stiffness and the local boundary conditions causing the stresses to change. Although, the stress change in multiple cells can give enough information if it is delaminated or not, its delamination area location is unknown. Surrogate models built upon Neural Networks (NN) and Finite Element Method (FEM) are developed to predict the out of plane stresses at the delaminated layer. FEM simulation models are calibrated with Moiré measurements and validated at the component and PCB level with stress difference measurements. Simulation delamination areas are constructed based on the Scanning Acoustic Microscope (SAM) images, and are also validated with the equivalent stress measurements. In the end the surrogate model is predicting the out of plane stress in the adhesive layer. The results show good correlation when compared to the SAM images.

1. Introduction

There are several definitions of Reliability [1,2]. In engineering [2], it is set as the “ability of a system or component to perform its required functions under stated conditions for a specified period of time”. These conditions refer to conditions like mechanical, thermal, electrical specifications. In this definition, a system [3] is “a combination of interacting elements (components) organized to achieve one or more stated purposes”.

Reliability prediction methods date 70 years into the past [4]. In that time, the concept of Reliability has been extensively used on design, operation and maintenance tasks. On the design stage of a product the concept of Design for Reliability (DfR) [5] appears, in which a model of the product is developed. This model is used by the manufacturer to define the working conditions and lifetime of the product that it will guarantee. A more reliable component (or system) works longer hours on tougher conditions on the operation stage; saving with this maintenance, repairs and replacement costs.

There are two main approaches in reliability: A statistic-based approach (like the Weibull model [6] or the fault tree analysis [7] that considers the reliability of each component to estimate the reliability of a system) or a physics-of-failure-based approach [5] (like the use of Finite Element Method (FEM) software to simulate loading conditions and ensure that the component will perform at its design capacity).

Both models do not predict the time instance status of a singular component. As neither monitors the dynamic state behavior of the component. Their assessments are of statistical relevance.

It is because of this that, for example, other techniques as redundancy are usually used to ensure zero Downtime (the period in which a system is unavailable) on relevant components. But this solution requires having another component identical in function as the original as backup and this solution is not cost-effective.

* Corresponding author at: Robert Bosch GmbH, Automotive Electronics, Reutlingen 72703, Germany.
E-mail address: alexandru.prisacaru@de.bosch.com (A. Prisacaru).

https://doi.org/10.1016/j.microrel.2021.114134
Received 22 December 2020; Received in revised form 3 April 2021; Accepted 16 April 2021
Available online 28 May 2021
0026-2714/© 2021 Elsevier Ltd. All rights reserved.

With this new notion and the foreseeable advent of widespread complex consumer grade systems as autonomous vehicles, it becomes evident that a new paradigm must be set to overcome the limitations of current reliability models.

This shift, the Digital Twin, integrates ultra-high fidelity simulations [8], historical data and machine learning models to mirror the physical object. Due to the fact that Digital Twin term is developed for a complex system, in this paper, we would like to propose the term Virtual Twin to represent the component part.

Therefore, this paper proposes the virtual twin of an electronic package using techniques like geometrical based simulations, experimental data and machine learning models.

2. Methodology

2.1. Machine Learning

ML should not be confused with Artificial Intelligence (AI). AI is the concept of a machine exhibiting intelligence similar to humans or animals. AI is divided into Weak and Strong AI. The former is an AI that can perform a narrowly defined set of tasks or just one task. The latter is an AI that is capable of applying intelligence to a problem and even showing consciousness. This means that the machine exhibiting Strong AI is not constrained to just one set of problem, as its knowledge and intelligence generalizes to all sets of tasks.

Strong AIs do not exist up to date. All current AIs are Weak as they specialize into solving a set of tasks tightly constrained and work using curated data sets, differing from the human learning experience.

ML is a subset of artificial intelligence (AI) that creates systems to learn and predict outcomes without manually programming a computer and is also known as predictive analytics or "statistical learning" [9]. It is a set of algorithms and techniques focused to learn from data. Here, data is an organized collection of measures and/or classes; and learning means the ability to get information from data that would generalize to other sets of data. This last is what differences ML techniques from other statistical tools. They focus on the generalization aspect of the data analysis and not only in creating a model that works with the data at hand. A ML model is *general*, it is valid for new data points the model has never been exposed to.

The miniaturization of computers carried an exponential growth in computational power that allowed ML models to be applicable, and in the later decades to become mainstream with open source projects as Scikit-learn, TensorFlow and PyTorch.

In this paper stress measurements during reliability test are recorded by an acquisition unit (AU) capable to send the data to a centralized data unit through a WiFi connection. Data stored in the Raspberry Pi is then sent to a server where data is processed. The data is transformed by removing the outliers, filtering, labeling and scaling. A ML regression technique is then applied to create a model to predict the out of plane stresses in the adhesive layer by feeding different delamination profiles simulation data. The model is then used to assess the out of plane stresses in the adhesive layer from the stress difference measurement data. It is a known that out of plane stresses are a direct indication where the delamination area is located. Therefore, the goal of this model is to give an indication where the delamination in the adhesive is located, not the magnitude of the stress values.

2.2. Surrogate modelling

The amount of cells provides a very good resolution of the stress difference distribution over the surface of the silicon die. However, to predict the delamination by just looking at the stress difference is not trivial, as discussed in the previous section. Machine learning is used to cope with this problem. In this paper, as an initial step a model is trained with the 21 delaminated simulation data with the stress difference as the input and σ_z at the interface between glue and silicon die as the output.

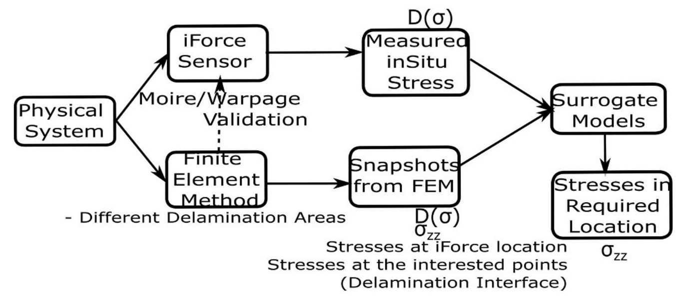

Fig. 1. Surrogate modelling.

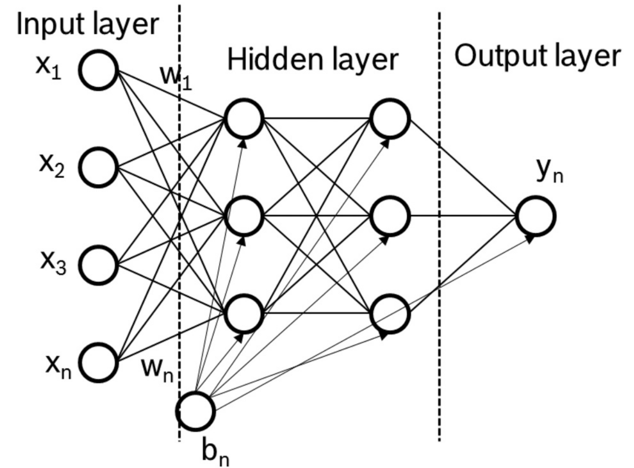

Fig. 2. Visual representation of an artificial neural network.

Virtual Twin by Surrogate modelling technique is shown in Fig. 1. FEM simulation snapshots are used to train the correlation between the stress difference on top of the silicon die and the out of plane stresses on the adhesive layer. Further, the trained NN is used to predict the out of plane stresses based on the measured stress difference from different delaminated TVs.

Nowadays there is a set of techniques that shines for their performance called Artificial Neural Networks (ANNs). A simple representation of a Feed-Forward Artificial Neural Network can be seen on Fig. 2. By themselves ANNs are not a method, but a tool to enable the collaboration between methods towards a common goal. An ANN is a collection of Artificial Neurons, therefore it is necessary to review what is it and what it does a single Artificial Neuron (AN).

ANs have been inspired in biology in the way it keeps a biological structure aiming to replicate a biological function[1] On Fig. 3 it can be seen a comparison between a biological neuron (3a) and an artificial neuron (3b).

The most basic model that can be used on an AN is a Perceptron. This linear model was invented by Frank Rosenblatt in 1958 [11].

Neural Networks consist of the following components:

- An input layer, x
- An output layer, y
- A set of weights and biases between each layer, W and b
- A choice of activation function for each hidden layer, σ

[1] This is a common practice in Engineering: In the same fashion the wing of a plane preserves its general structure, replicating a specific function of a biological wing. ANs keep the structure of biological neuron and aims to loosely replicate the biological function of a biological neuron.

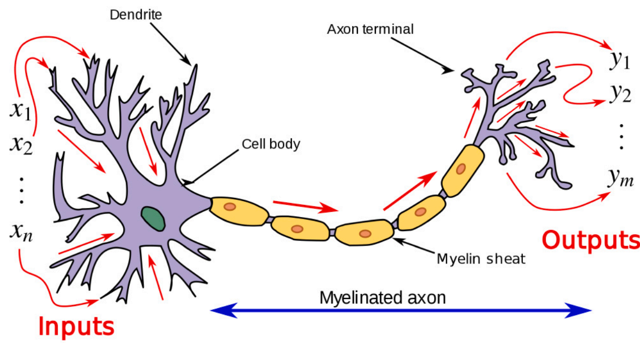

(a) Biological neuron [10].

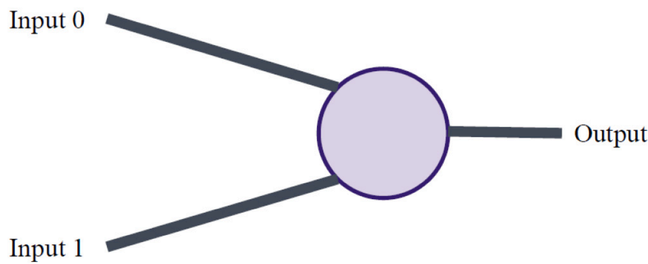

(b) Artificial Neuron.

Fig. 3. Comparison between biological [10] and artificial neurons.

Having a set of data points organized in the matrix X that is formed by individual data points vectors x. The model comprises a mathematical function as in eq. 1.

$$y(x) = f(w \times x) + b \tag{1}$$

This means, if we know weight matrix w and bias vector b, under the chosen activation function f, we can predict unknown output value y, by known input vector x. Input vector x is always known, so how to get weight matrix w, and the bias vector b becomes the key problem, which is exactly the purpose of ANN training purpose.

Most used activation functions are step, sign, sigmoid,[2] tanh[3] and ReLU[4]:

$$step(z) = \begin{cases} 1 & \text{if } z \geq 0; \\ 0 & \text{if } z < 0. \end{cases} \tag{2}$$

$$sign(z) = \begin{cases} 1 & \text{if } z \geq 0; \\ -1 & \text{if } z < 0. \end{cases} \tag{3}$$

$$sigmoid(z) = \frac{1}{1 + e^{-z}} \tag{4}$$

$$tanh(z) = \frac{e^z - 1}{e^z + 1} \tag{5}$$

$$ReLU(z) = max(0, z) \tag{6}$$

$$identity(z) = z \tag{7}$$

The selection of the activation function depends on what type of behavior the perceptron is designed to abstract from the data that will feed it. Like this, a perceptron with a sign activation function would be used for linear classification tasks, a perceptron with an identity activation function would be used for linear regression and a perceptron with a sigmoid activation function would be used for logistic regression.

Backpropagation (BP) is a method used in artificial neural networks to calculate the error contribution of each neuron after a batch is processed. This is used by an enveloping optimization algorithm to adjust the weight of each neuron, completing the learning process for that case. We predict the input part of training data by the current neural network, this is usually called forward propagation. And we get a set of output data, which has differences with the output part of the training data, this is error. In optimization algorithm, this error is named loss function, our goal is to optimize the parameters of the network to make the loss function reach its minimum point. Which means the neural network fit the training data and can represent the real model. Technically it calculates the gradient of the loss function to reach the optimization goal. It is commonly used in the gradient descent optimization algorithm. It is also called backward propagation of errors, because the error is calculated at the output and distributed back through the network layers to adjust all the parameters inside the network. This BP method has limitations, because it is gradient based optimization method, so BP is not guaranteed to find the global minimum of the loss function, maybe just a local minimum. This can be solved by making some improvements, such as:

- add momentum factor to make learning rate adaptive
- training more times, then we may get the global minimum at larger probability
- combining other optimization algorithms into BP, for example Particle Swarm Optimization, Genetic algorithm, etc.

Learning rate can be regarded as improvement step, represent how far we take the next step towards the negative gradient direction. If this value is big, we only need several steps (iterations) to approach the minimum point, which means faster convergence and time saving. There are many rule-of-thumb methods for determining an acceptable number of neurons to use in the hidden layers, such as the following: the number of hidden neurons should be between the size of the input layer and the size of the output layer. Momentum factor it can be regarded as an adjustment of the learning rate, to make the step length no longer fixed, thus can realize large steps at beginning to make loss function drop fast, and shrink the step when approaching the minimum.

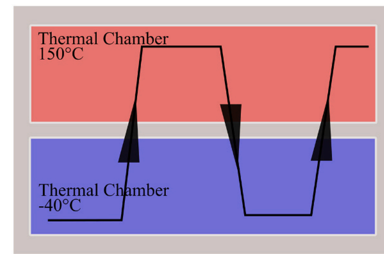

Fig. 4. Thermal chamber procedure description.

3. Experiment

Accelerated reliability testing are used to stress the Test Vehicles (TV). In this study air thermal shock chamber was used, which consists in two separate chambers with constant temperature, one at 150° and the other one at −40° as shown in Fig. 4. The basket containing the TVs is moving up and down between chambers. The transition time between chambers is relatively small making the experiment suitable to accelerate the degradation of the electronic packages.

The dwelling time was predetermined to provide a condition where all components reach the uniform distribution at target temperatures.

[2] Also called logistic function.
[3] Hyperbolic tangent function.
[4] Rectified linear unit.

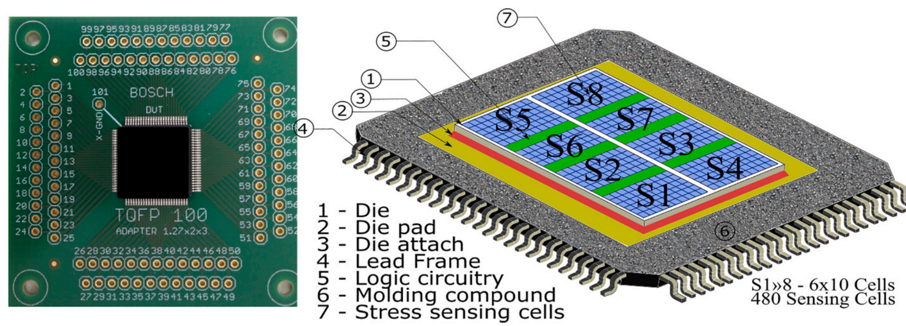

Fig. 5. TQFP mounted on a PCB test vehicle.

3.1. Test vehicle

Thin Quad Flat Packages (TQFP) 100 × 100 pins with encapsulated piezoresistive silicon based stress sensor are mounted on a PCB. This is a standard package for automotive industry in application specific integrated circuit (ASICs). They are mostly used for vehicle airbags, engine management, transmission control system, advanced driver assistance systems, in-vehicle communication and alternator electronics. As shown in Fig. 5 the functional die is replaced by the stress sensor die.

The package silicon die consists of 8 sensors, with 60 stress measuring cells each, having a total of 480 stress sensing cells. The packages were specially designed to have low adhesion strength between the leadframe and the molding compound. One of the way to do this was to use oxidized leadframes in the packaging process. Also, two molding compounds were used for packaging MC1 and MC2. In total six TVs were tested by performing two separate experiments. Two TV are of type 1 molding compound $MC1_1$, $MC1_2$ and another four of type 2 molding compound $MC2_1 \ldots MC2_4$, respectively. In this paper $MC1_1$ sample is used to show the stress difference, simulation out of plane stress distribution and the SAM images in case of delamination.

3.2. Stress evaluation

In TQFP stress sensors are encapsulated as a regular die to record the mechanical stresses during reliability tests. In this paper TQFP contains 8 sensors with each 6 by 10 stress sensing cells. To evaluate the stresses the following formulas have been used.

The relationship between measured currents and stresses are:

$$D(\sigma) = \sigma_{xx} - \sigma_{yy} = \frac{1}{\pi^p_{44}} \frac{I_{OUT} - I_{IN}}{I_{OUT} + I_{IN}} \tag{8}$$

$$\sigma_{xy} = \frac{1}{\pi^n_{11} - \pi^n_{12}} \frac{I_{OUT} - I_{IN}}{I_{OUT} + I_{IN}} \tag{9}$$

where $\pi_{11}, \pi_{12}, \pi_{44}$ are the piezoresistive coefficients of silicon; and I_{IN}, I_{OUT} are the currents measured at the input and output of the sensor, respectively. More details can be found in Ref. [12–14].

After the experiments were performed, data was processed and only one measurement point per cycle is extracted at the dwell time. Then the stress values at -40° are extracted from the values at 150° as follows:

$$D(\sigma)^{rel}_{ij} = \left(\sigma_{xx} - \sigma_{yy}\right)^{-40^\circ C} - \left(\sigma_{xx} - \sigma_{yy}\right)^{150^\circ C} \tag{10}$$

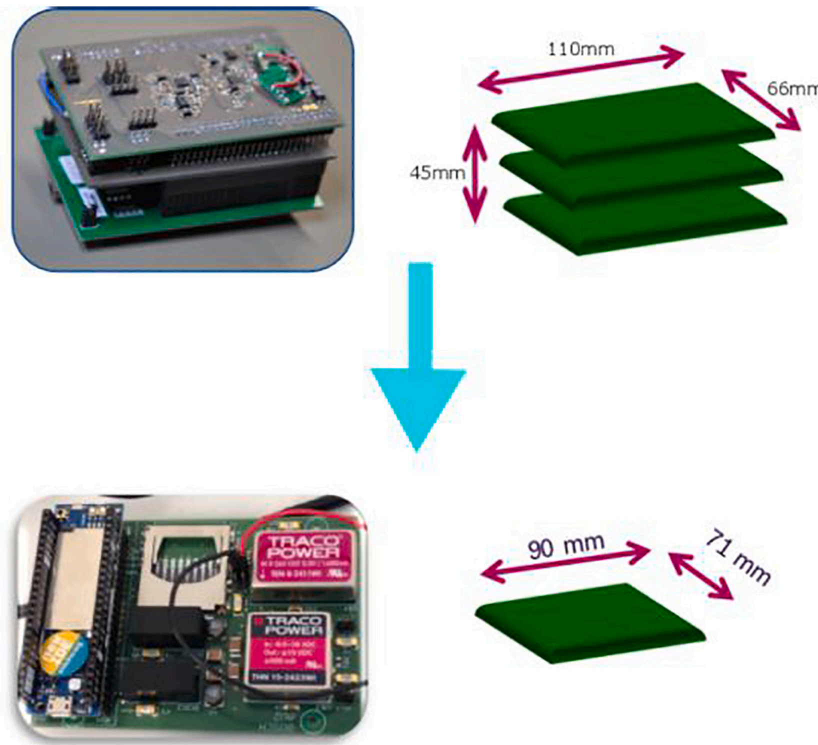

Fig. 6. Acquisition unit downsize.

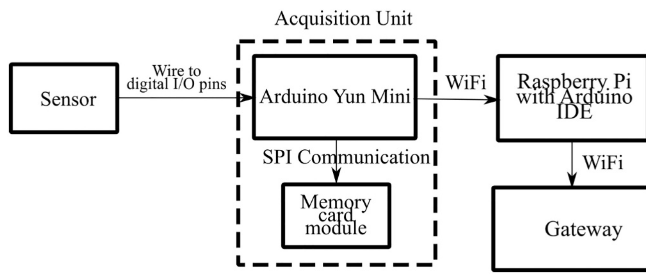

Fig. 7. Data flow.

where i=1,..,n is the number of measurement points, j=1,…, 480 is the number of sensing cells and $D(\sigma)_{ij}$ are the relative stress difference.

3.3. Acquisition unit

A dedicated acquisition unit was used to power, steer and acquire data from the stress sensor. Additional improvements has been made to the AU to facilitate efficient experiments. In terms of dimension, and weight, the former AU is consisted by three board, it is 110 × 66 × 45 mm in size. The new AU has only one board, its size is 90 × 71 × 20 mm. Shown in Fig. 6.

In terms of speed, the former acquisition unit consumes several minutes to collect data from 480 cells (8 sensor × 60 cells/sensor), at 12 bit accuracy. The new acquisition unit has two ADCs, ADS1115 and ADS1015, by changing I2C slave address value in I2C library, one can choose between two ADC. When ADS1115 chosen, we can get 16 bit accuracy, but it requires more time to go through all 480 cells; When choose ADS1015, we still have 12 bit accuracy data, but faster measurements. As for other functions, the new one has built-in WIFI module that facilitates the connection with Raspberry Pi, and the wireless data transmission through WIFI is realized; Pi was also added, because stress value calculation method, stress prediction algorithms based on Neural Network (NN), are all coded in Python and can run on Raspberry Pi. That is to say, Pi is a microcomputer which can afford all the functions in this task, and it is of course lighter, cheaper, more convenient, and mobile than a PC. Meanwhile, real time data processing becomes possible, because WIFI connection can realize real time data transmission between Pi and Arduino.

By realizing wireless WIFI connection between Arduino and Pi (see Fig. 7), we can imagine that Pi can communicate with multiple Arduinos at same time. Pi has the ability to generate its own network as a hot spot, and Arduinos can have access to the hot spot, thus build the grid that multiple Arduino transmit data to a common central process Pi. So we can realize the in-situ stress monitoring on multiple sensors and AU by one Pi.

3.4. Delamination validation through SAM images

SAM image of the sample was recorded at 0 cycles, 1050 Cycles and at the end. This can help in correlating between the stress difference values and delamination. In Fig. 8 SAM images of the TQFP package targeting the interface between copper pad/molding compound, die attach/copper pad and die/die attach are shown. One image was performed at the beginning of the test, showing no initial delamination. An intermediate picture at 1050 Cycles, where initial delamination is detected, was performed. The third picture was performed after 2500 temperature cycles and more than 80% of delamination is found.

3.5. Data from thermal cycling data

The in-plane mechanical stresses were recorded during the entire test for all the 480 measuring cells. The AUs were placed outside the chamber with a wire connection with the samples inside. For visualization purposes average relative stress changes are calculated by averaging over 480 cells as follows:

$$D(\sigma)_j^{average} = \sum_{1}^{480} D(\sigma)_{ij}^{rel} \tag{11}$$

The influence of delamination in the die attach over the stress difference on top of the die is shown in Fig. 9. An average value of stress per cycle is depicted by using eq. 11. The first observation is that the stress values completely change after 900 Cycle reaching a maximum change at 1300 Cycle. The stress variation corresponds to the local boundary

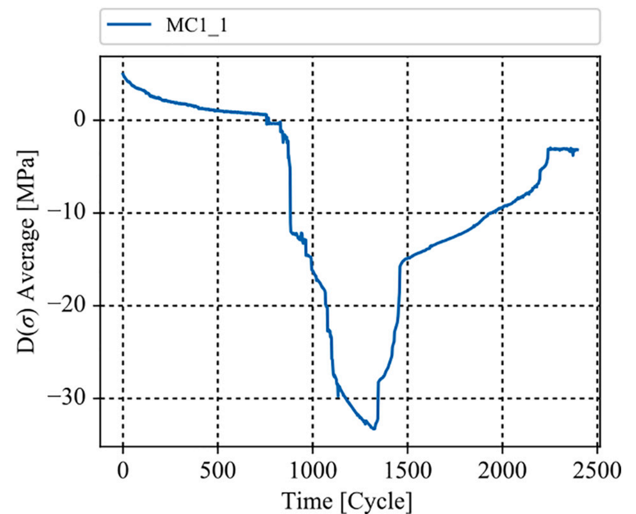

Fig. 9. Normal in-plane relative stress difference average along all 480 Cells for MC1_1 Sample.

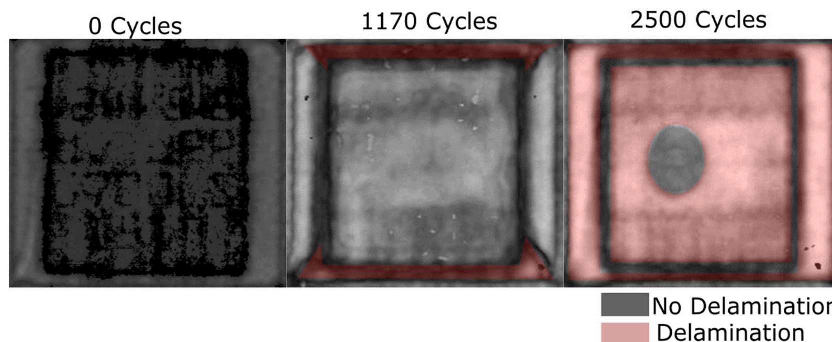

Fig. 8. MC1_1 TV SAM image before and after the reliability test. The delamination area is shown in red colour.

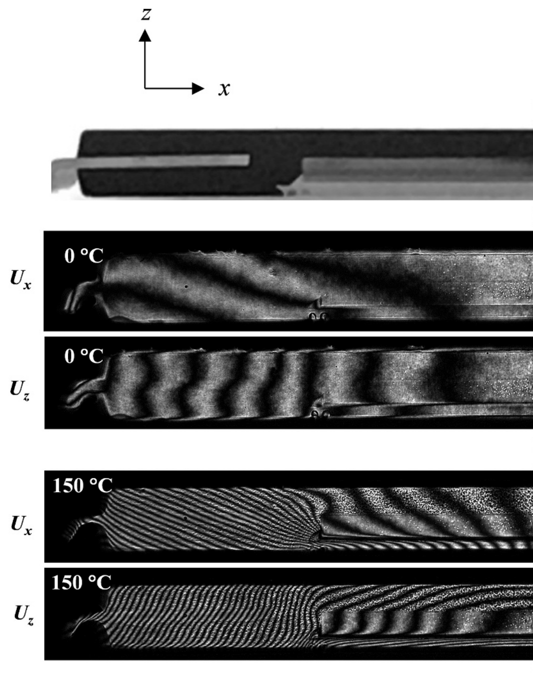

Fig. 10. *Ux* and *Uz* displacement fields of the left-half of the TQFP obtained at 0° and 150°.

condition changes. The absolute high values of stress are driven by the high stresses in the region close to the crack. The delamination is confirmed by the SAM image taken at 1050 cycle. For a better understanding of the stress signal given by the delamination an FEM model is constructed. More details regarding the experiment can be found in [15].

3.6. Thermal deformation with Moiré interferometry

Real-Moiré interferometry was utilized to improve the prediction accuracy of FEM simulation. The method is a full-field optical technique to measure the in-plane deformations with high sensitivity, high signal-to-noise ratio, and excellent clarity [16]. The outputs are the contour maps of in-plane displacements. It has been used widely for electronic packaging design and reliability assessment [17]. The optical/mechanical configuration used in the study consists of (1) a portable engineering moiré interferometer that provides two sets of virtual reference gratings and (2) a conduction chamber built on a high performance thermoelectric cooler that provides accurate temperature control. More details about the test setup can be found in [18].

A cross-line diffraction grating with a frequency of 1200 lines/mm was replicated on the specimen surface at room temperature (20°). The specimen was placed inside the thermal chamber and was subjected to a thermal excursion. The specimen grating deformed together with the specimen to produce two orthogonal in-plane displacement fields. The details about the grating and replication procedures can be found in [16,19]. The in-plane *Ux* and *Uz* displacement fields, obtained at 0° and 150°, are shown in Fig. 10, where the top figure shows the left-half of the TQFP on which the grating was replicated.

4. Results and discussion

4.1. Simulation data

A simulation data set is extracted from Finite Element Method (FEM) simulations. It is composed by 21 different thermo-mechanical simulations considering different delamination profiles constructed based on

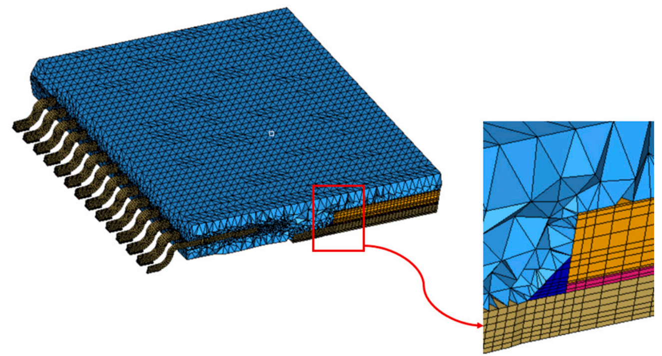

Fig. 11. Detail on FEM mesh of a quarter model TV TQFP.

Table 1
Material properties.

Component	Young's [*GPa*]	Poisson's ratio Modulus	CTE below T_g [*ppm/K*]	T_g [*°C*]
Outer Mold	22÷32	Below T_g:0.25÷0.3 Above T_g:0.4÷0.46	8÷11E−06 2÷3E−05	90÷110
Lead Frame	75,000	0.343	1.7E−05	–
Stress Sensor	x:168.9E+03 y:168.9E+03 z:130.2E+03	ν_{xz}:0.064 ν_{xy}:0.361 ν_{yz}:0.361	2.8E−06	–
Die attach	7632	below T_g:0.35 above T_g:0.45	5.10E−05 1.71E−04	37.55

the SAM images. The FEM model simulations is performed using ANSYS sparse solver with more than 1.5 million elements mesh.

A detail on the model is shown on Fig. 11. On the zoom image to the right, can be seen:

- On the lower side on beige colour its located the copper heat dissipator.
- On top of the heat dissipator on orange colour there is the silicon die. On the top face of the die is where the sensing cells are located.
- Between the heat dissipator and the silicon die, there is glue on magenta colour.
- On the side, the connection terminals are shown on beige colour. These are connected with wires to the sensors on top of the silicon die.
- On the four sides of the die additional glue can be seen on colour blue.
- Around the die, and containing one end of the connection terminals, it is the molding compound on cyan colour.

A visualization of the mesh of the model is shown on Fig. 11. The molding compound is modelled using second order solid tetrahedral elements. All other regions are modelled using second order solid hexahedral elements. The thickness of the silicon die in the actual sensor chip was discretized with a layer of approximately 10 μm thick. Each stress sensing cell was divided into 4 × 4 elements so that the elements matched to the geometry of the sensor itself (More details can be found in [14]). Material properties used in the simulation are shown in Table 1.

Moiré measurements are used to calibrate the component simulation model. Optislang software is used to run an optimisation task to minimise the root mean square error between the moiré measurements and simulation. Ranges in values of Young's Modulus, Poisson's ratio, coefficient of thermal expansion and glass transition temperature of the molding compound are therefore chosen as shown in Fig. 1. Displacements extracted on x and z direction along a horizontal line in the simulation are extracted and can be depicted in Fig. 12a, b. A good agreement between simulation and measurements can be seen after the

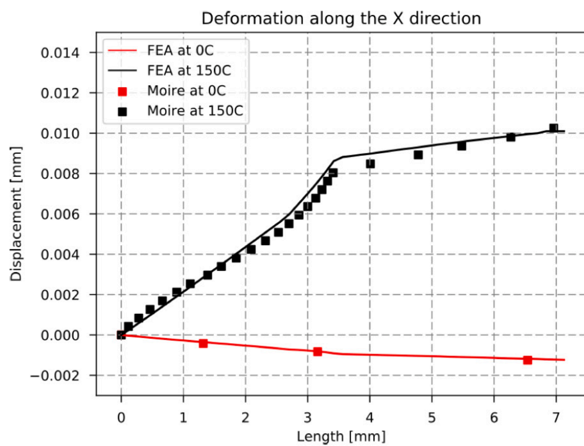

(a) Ux displacement along x direction. Simulations vs. Moiré measurements.

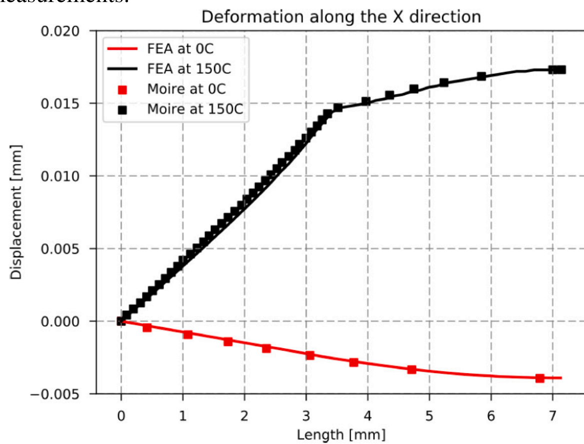

(b) Uz displacement along z direction. Simulations vs. Moiré measurements.

Fig. 12. FEM ETV model.

optimization task is performed. A quarter model is built with half symmetry along one direction and free surface along the other direction as boundary conditions. The moiré data is extracted along the free surface, which corresponds to the cut in the TQFP. Simulation results are extracted at $0^{\circ}C$ and $150^{\circ}C$ with the corresponding room temperature reference.

A second validation is performed on a component level TQFP to establish the agreement between stress measurements and simulation. This is also a reference for how the stress distribution looks like in the healthy samples. Then the simulation is updated with the printed circuit board (PCB) to mimic the reliability TV.

The values of relative stress along the x and y direction on top of the die and the stress difference calculation for the TQFP component alone from the simulation are shown in Fig. 13. This can give us a better understanding of what the sensor can measure, which is the stress difference.

The modelling predictions are compared with the measured stress difference data from a component alone in Fig. 14. The results show good agreement. The deviations are attributed to the uncertainties of the stress sensor, geometry imperfections (variations) and the material properties used in the simulation. It is worth mentioning that the minimum and maximum values of stress difference are located near the edges.

PCB level delaminated TQFP simulation is constructed based on the SAM image shown in Fig. 8. The stress values along x and y direction when the delamination is present, is depicted in Fig. 15. This visualization has the purpose to show the link between delamination, the stresses along x and y direction and the stress difference. Also, this is an efficient indication that the stress difference values are able to capture the delamination.

The same amount of contact area shown in the SAM image (Fig. 8) is used for modelling the delamination in the simulation. In the area where delamination is considered, the interface mesh node is divided in two mesh node with no connection. In the other areas node to node connectivity is maintained.

Fig. 16 shows the contour plot of the relative stress difference from both simulation and measurement with the designated delamination area shown in the SAM image. In this case the agreement between the measurement and the simulation in the undelaminated area shows the limitation of the method used in case of simulating the delamination area. Both plots show similar stress distribution where the undelaminated area is present. The distribution near the undelaminated area is similar as in the case of Fig. 14. Overlay pictures between the stress difference and SAM image of both simulation and measurement are shown in Fig. 17. The top/bottom and left/right stress distribution of maximum and minimum values are exactly on top of the edge of the undelaminated area.

Although the stress difference is giving an indication where the delamination areas are present, these are visible only when the package is fully delaminated. When the delamination areas are closer to the edges of adhesive layer, it is visually difficult to estimate where the delamination is located. One such examples is depicted in Fig. 18. Therefore, one more intermediate step is needed to reveal the delamination areas.

From the FEM simulation is observed that σ_z extracted at the adhesive layer describes the delamination area much better, as depicted in Fig. 19. The image shows a top view on the model, where the grey colour represents the delaminated area and the red undelaminated area respectively.

The simulation dataset contains the values of $D(\sigma)_{ij}^{rel}$ on each element on the top face of the silicon die, where the sensing cells would be

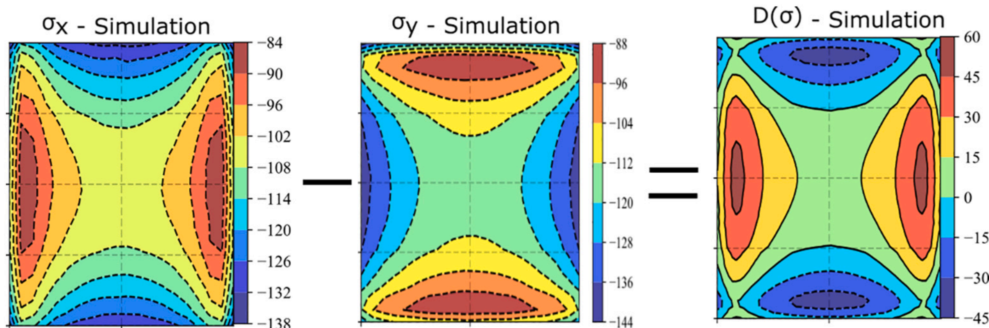

Fig. 13. TQFP component level mechanical stress at the top of the die. Loading condition used in the simulation is an environmental temperature of -40° and 150°. The stress values at -40° are extracted from 150° stress values.

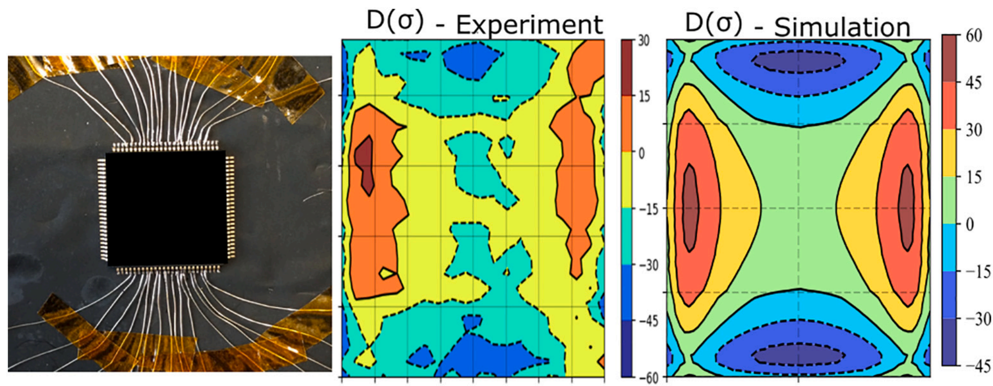

Fig. 14. TQFP component level mechanical stress at the top of the die measured vs. simulation. Loading condition used in the simulation and measurement is an environmental temperature of −40° and 150°. The stress values at −40° are extracted from 150° stress values.

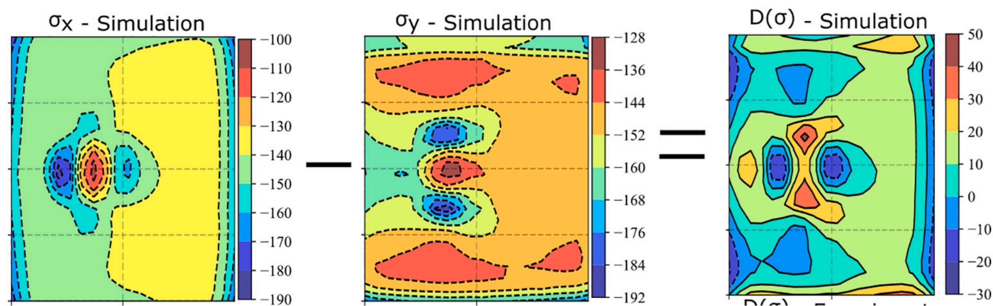

Fig. 15. Simulation mechanical stress at the top of the die of the delaminated *MC*1_1 TV. Loading condition used in the simulation is an environmental temperature of −40° and 150°. The stress values at −40° are extracted from 150° stress values.

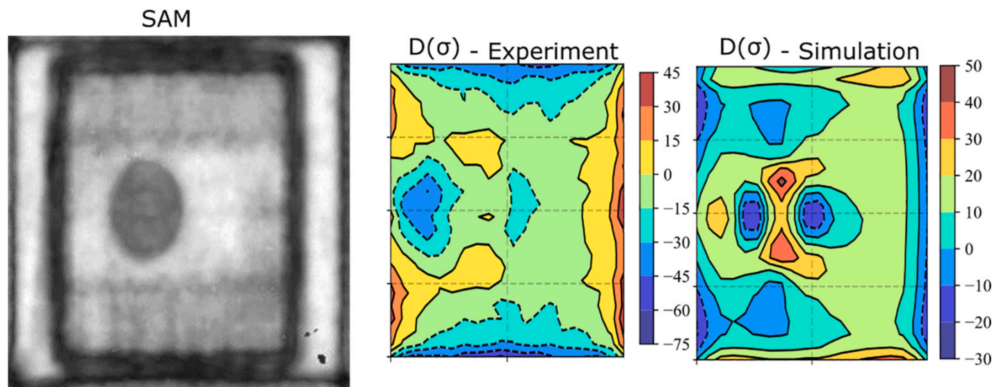

Fig. 16. Simulation and measured mechanical stress difference at the top of the die of the delaminated *MC*1_1 TV. Loading condition used in the simulation is an environmental temperature of −40° and 150°. The stress values at −40° are extracted from 150° stress values.

located, and σ_z of all elements on the lower side of the silicon die. The element geometry has been designed so the top and lower faces contain a 2*3 array of mesh elements. In total 21 simulations are performed containing different delamination areas based on the SAM images taken during and at the end of the reliability tests.

The simulation returns two types of data:

- $D(\sigma)_{ij}^{rel}$ on the top face of the silicon die: The simulation gives as output the relative stress difference between the peak low temperature and the peak high temperature. With this values per element, visualizations as in Fig. 16 can be created.
- σ_z on the lower face of the silicon die: The simulation calculates the σ_z. A visualization of one of this images is shown in Fig. 19.

As depicted in Fig. 19, σ_z describes the delamination well in comparison to the $D(\sigma)_{ij}^{rel}$, where it is hard to make a visual correlation between the stress and delamination. Therefore, the values of predicted σ_z are chosen as a virtual sensor to show where the delamination area is located.

4.2. Back propagation artificial neural network

For our application the input data contains the relative stress difference from all the 480 cells from 21 simulation data. The output data contains σ_z from all the corresponding 480 cells on the interface with the glue.

A Surrogate Model is the one that is constructed using a model of the outcome that is looked upon instead of real-world measures. This

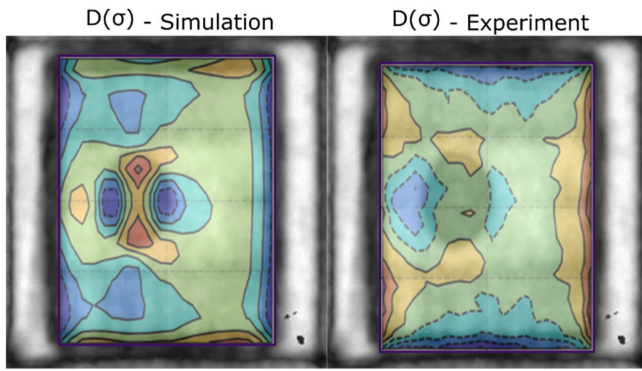

Fig. 17. *MC*1_1 TV overlay picture of stress difference on top of SAM image. Both simulation and experiment gives a very good indication where there is still contact underneath the die.

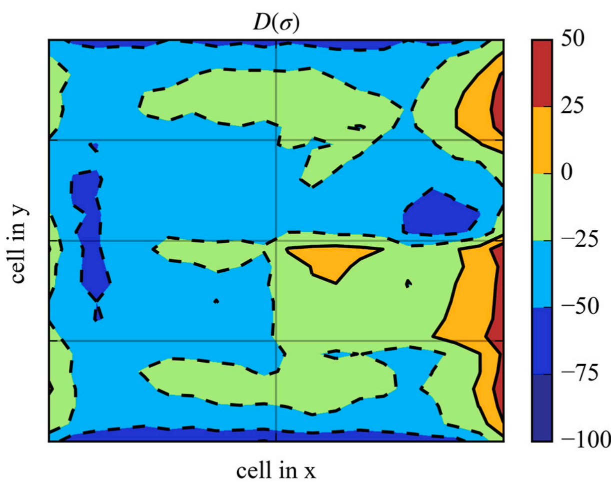

Fig. 18. *MC*1_1 TV stress difference at 1400 cycle.

technique is used when the real world measures are impossible to obtain (like in the case of theoretical physics models), are computationally expensive (for example for complex FEM simulations) or a precise physical measures are hard to obtain (out of plane stresses in our case).

Because of the few amount of data points, this model will be trained with the whole simulation data set that includes all 21 delamination profiles and then the results will be evaluated using SAM scans of the last state of the TVs. The input is a 480 signal corresponding to the 480 stress difference signals of the sensors that would be located on the top of the silicon of the TV, and the output is a 480 signal corresponding to the σ_z on the locations directly opposite to them on the other side of the silicon (interface with adhesive).

The BPNN architecture is as shown on Table 2:

A summary of the results obtained is shown in the appendix in Fig. 20. On these images, the output corresponding to the last thermal cycle of the modules experimental data sets is shown besides the SAM scan of its last state for comparison. A visual examination shows that the simple network created with the small simulation dataset has been able to predict until certain degree the final delamination state of the TV. The maximum values of out of plane stresses are located at the boundary between the delaminated and not delaminated area, seen in the SAM images.

In Fig. 20d it is observed that the σ_z prediction reveals the delamination area is located around the edge of the adhesive layer. This is validated by the SAM image. In this current form, the NN algorithm tries to fit the measurement data to one of the delamination profiles given to the simulation. It is therefore not able to interpolate between the delamination areas. A generalization of this model is therefore possible, only when a sufficient delamination profiles data are available from the simulation. A time discrete approach to establish a Virtual Twin model for an electronic component is required.

5. Conclusions

In this paper, a surrogate model based on simulated in-plane and out of plane stress is proposed. Mechanical stresses are able to capture structural change in the packages including delamination. The BPNN model shows promising results to estimate the delamination areas inside the package. The neural network is fitting the data to one of the provided delamination profiles. If the model contains sufficient discretized

Table 2
BPNN parameters.

Parameter	Value
Hidden layers	[100,]
Activation function	ReLU
Solver	SGD
Learning rate	0.0001
Max iterations	2200
Tolerance	0.0005
Max iterations under tolerance	30
Momentum	0.1

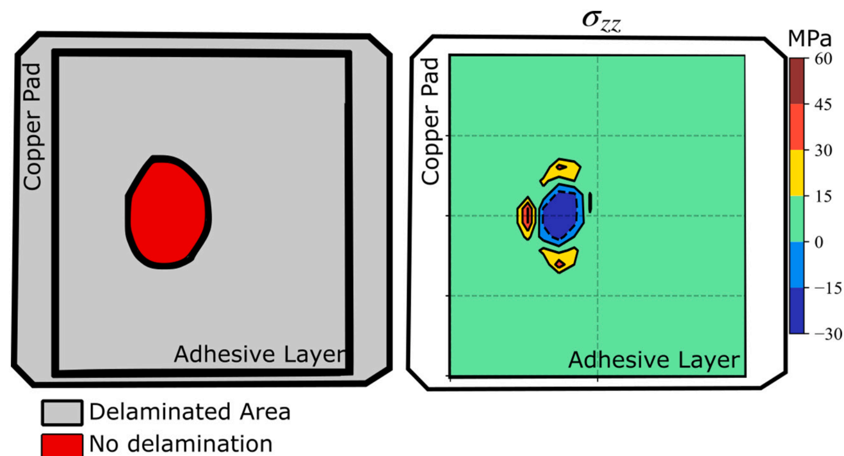

Fig. 19. Delaminated area versus σ_z on simulation dataset. Grey area represents the delaminated area and in the simulation is given as a no contact interface. The red area represents no delaminated area and in the simulation is given as a bonded contact interface.

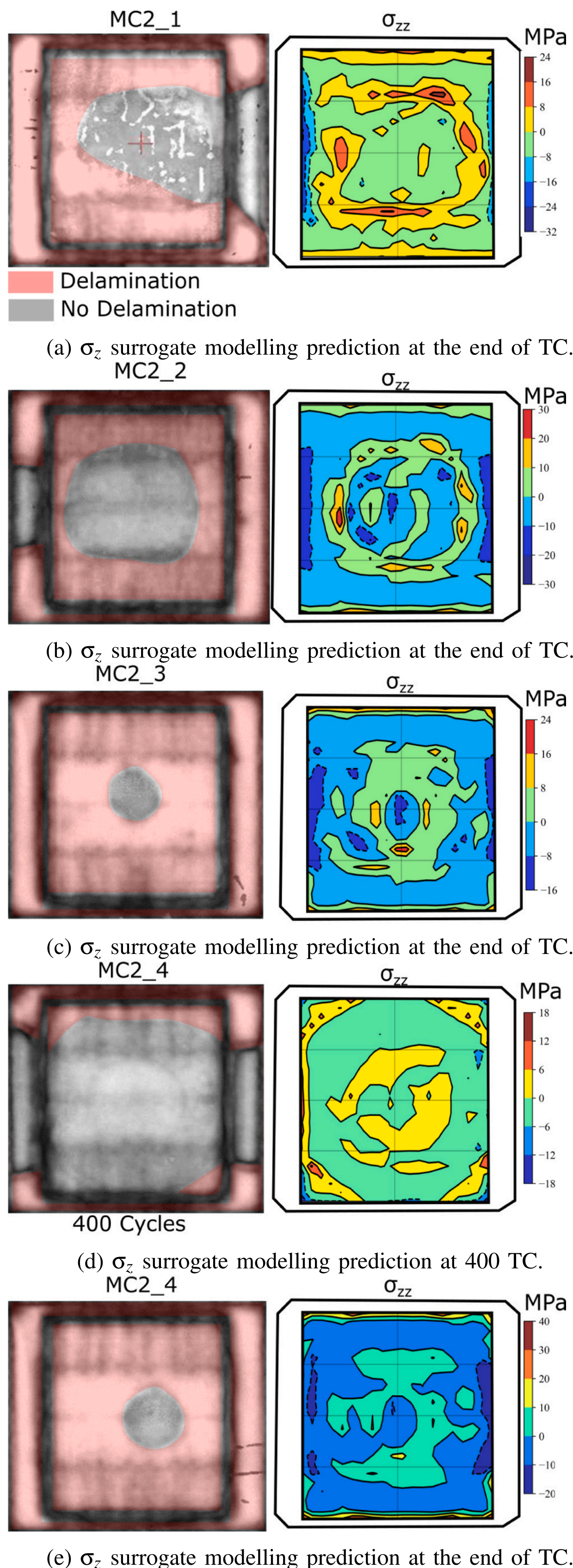

(a) σ_z surrogate modelling prediction at the end of TC.

(b) σ_z surrogate modelling prediction at the end of TC.

(c) σ_z surrogate modelling prediction at the end of TC.

(d) σ_z surrogate modelling prediction at 400 TC.

(e) σ_z surrogate modelling prediction at the end of TC.

Fig. 20. SAM images versus the surrogate modelling predictions.

delamination profiles, then the model can be more accurate. This non-intrusive method can be used in testing new package designs, which can lead in better and fast design. Also, has the potential to be used in Digital Twin for automotive electronics as virtual sensors. Future work should be focused in acquiring more testing data for different designs and implementing more efficient FEM and ML methods.

CRediT authorship contribution statement

Alexandru Prisacaru – Conceptualization, Methodology, Software, Writing - Original Draft, Writing - Review & Editing, Visualization.
Ernesto Oquelis Guerrero – Software, Data curation.
Balakrishna Chimmineni - Simulation.
Przemyslaw Jakub Gromala – Conceptualization, Validation, Supervision, Funding acquisition.
Yu-Hsiang Yang - Validation.
Bongtae Han – Conceptualization, Validation, Supervision.
Guo Qi Zhang – Conceptualization, Supervision.

Declaration of competing interest

The authors declare that they have no known competing financial interests or personal relationships that could have appeared to influence the work reported in this paper.

Acknowledgements

The work was funded by the Federal Government of Germany, Framework Program for Research and Innovation 2016–2020 Microelectronics - Innovation Drivers of Digitalization (Rahmenprogramm der Bundesregierung für Forschung und Innovation 2016–2020 Mikroelektronik aus Deutschland - Innovationstreiber der Digitalisierung) - Project smartSTAR (No. 16ES0965). This funding is gratefully appreciated. Many thanks to all members of the project team for the good cooperation.

References

[1] Seyedmohsen Hosseini, Kash Barker, Jose E. Ramirez-Marquez, A review of definitions and measures of system resilience, Reliab. Eng. Syst. Saf. 145 (2016) 47–61.
[2] 24765, ISO/IEC/IEEE International Standard - Systems and Software Engineering–Vocabulary - IEEE Standard, 2017.
[3] Claus Ballegaard Nielsen, Peter Gorm Larsen, John Fitzgerald, Jim Woodcock, Jan Peleska, Systems of systems engineering: Basic concepts, model-based techniques, and research directions, ACM Comput. Surv. 48 (2) (September 2015), 18:1–18:41.
[4] W. Denson, The History of Reliability Prediction 47(3), 1998, pp. SP321–SP328.
[5] Dana Crowe, Alec Feinberg, Design for Reliability, in: Volume 7 of Electronics Handbook Series, CRC Press, April 2001, https://doi.org/10.1201/9781420040845.
[6] M. Xie, C.D. Lai, Reliability analysis using an additive weibull model with bathtub-shaped failure rate function, Reliab. Eng. Syst. Saf. 52 (1) (1996) 87–93.
[7] H. Tanaka, L.T. Fan, F.S. Lai, K. Toguchi, Fault-tree Analysis by Fuzzy Probability R-32(5), 1983, pp. 453–457.
[8] Edward Glaessgen, David Stargel, The Digital Twin Paradigm for Future NASA and U.S. Air Force Vehicles, 04 2012.
[9] A.C. Mueller, S. Guido, Introduction to Machine Learning With Python: A Guide for Data Scientists, first edition, O'Reilly Media, Inc, 2016 (OCLC: ocn895728667).
[10] Prof. Loc Vu-Quoc, Neuron3, 2018 [Online; accessed 6th of January, 2019].
[11] F. Rosenblatt, The perceptron: a probabilistic model for information storage and organization in the brain, Psychol. Rev. (1958) 65–386.
[12] Alexandru Prisacaru, Alicja Palczynska, Przemyslaw Jakub Gromala, Bongtae Han, Guo Qi Zhang, Condition monitoring algorithm for piezoresistive silicon-based stress sensor data obtained from electronic control units, in: 2017 IEEE 67th Electronic Components and Technology Conference (ECTC), 2017, pp. 1119–1127.
[13] Alicja Palczynska, Alexandru Prisacaru, Przemyslaw Jakub Gromala, Bongtae Han, Dirk Mayer, Tobias Melz, Towards prognostics and health monitoring: The potential of fault detection by piezoresistive silicon stress sensor, in: 17th International Conference on Thermal, Mechanical and Multi-physics Simulation and Experiments in Microelectronics and Microsystems (EuroSimE), IEEE, 2016, pp. 1–8.
[14] A. Prisacaru, A. Palczynska, P. Gromala, B. Wu, B. Han, G. Zhang, Accuracy of cmos-based piezoresistive stress sensor for engineering applications of thermal

loading condition: theoretical review and experimental validation, IEEE Sensors J. 19 (20) (2019) 9139–9148.
[15] A. Prisacaru, P.J. Gromala, B. Han, G.Q. Zhang, Degradation estimation and prediction of electronic packages using data driven approach, IEEE Trans. Ind. Electron. (2021) 1.
[16] B. Han, D. Post, P. Ifju (Eds.), High Sensitivity Moire: Experimental Analysis for Mechanics and Materials, Springer-Verlag, 1997.
[17] B. Han, Thermal stresses in microelectronics subassemblies: quantitative characterization using photomechanics methods, J. Therm. Stresses (2003) 583–613.
[18] B. Wu, B. Han, Advanced mechanical/optical configuration of real-time moire interferometry for thermal deformation analysis of fan-out wafer level package, IEEE Trans. Compon. Packag. Manuf. Technol. 8 (5) (2018).
[19] B. Han, Recent advancements of moire and microscopic moire interferometry for thermal deformation analyses of microelectronics devices, Exp. Mech. 38 (1998) 278–288.